PAPER • OPEN ACCESS

Effect of tracer size distribution on magnetic particle imaging performance

To cite this article: Ebrahim Azizi *et al* 2025 *Phys. Scr.* **100** 025529

View the article online for updates and enhancements.

Physica Scripta

PAPER

Effect of tracer size distribution on magnetic particle imaging performance

Ebrahim Azizi[1] , Bahareh Rezaei[1] , Shahriar Mostufa[1] , Shuang Liang[2] , Yongqiang Andrew Wang[3], Vinit Kumar Chugh[4] , Jian-Ping Wang[2,4] , Changzhi Li[1] , Jenifer Gómez-Pastora[5] , Rui He[1] and Kai Wu[1]

1   Department of Electrical and Computer Engineering, Texas Tech University, Lubbock, TX, 79409, United States of America
2   Department of Chemical Engineering and Materials Science, University of Minnesota, Minneapolis, MN, 55455, United States of America
3   Ocean Nano Tech LLC, San Diego, CA, 92126, United States of America
4   Department of Electrical and Computer Engineering, University of Minnesota, Minneapolis, MN, 55455, United States of America
5   Department of Chemical Engineering, Texas Tech University, Lubbock, TX, 79409, United States of America

E-mail: kai.wu@ttu.edu

Abstract

Magnetic particle imaging (MPI) is a tracer-based tomographic imaging technique utilized in applications such as lung perfusion imaging, cancer diagnosis, stem cell tracking, etc. The goal of translating MPI to clinical use has prompted studies on further improving the spatial-temporal resolutions of MPI through various methods, including image reconstruction algorithm, scanning trajectory design, magnetic field profile design, and tracer design. Iron oxide magnetic nanoparticles (MNPs) are favored for MPI and magnetic resonance imaging (MRI) over other materials due to their high biocompatibility, low cost, and ease of preparation and surface modification. For core–shell MNPs, the tracers' magnetic core size and non-magnetic coating layer characteristics can significantly affect MPI signals through dynamic magnetization relaxations. Most works to date have assumed an ensemble of MNP tracers with identical sizes, ignoring that artificially synthesized MNPs typically follow a log-normal size distribution, which can deviate theoretical results from experimental data. In this work, we first characterize the size distributions of four commercially available iron oxide MNP products and then model the collective magnetic responses of these MNPs for MPI applications. For an ensemble of MNP tracers with size standard deviations of σ, we applied a stochastic Langevin model to study the effect of size distribution on MPI imaging performance. Under an alternating magnetic field (AMF), i.e., the excitation field in MPI, we collected the time domain dynamic magnetizations (M-t curves), magnetization-field hysteresis loops (M-H curves), point-spread functions (PSFs), and higher harmonics from these MNP tracers. The intrinsic MPI spatial resolution, which is related to the full width at half maximum (FWHM) of the PSF profile, along with the higher harmonics, serve as metrics to provide insights into how the size distribution of MNP tracers affects MPI performance.

1. Introduction

Magnetic particle imaging (MPI) is a new medical imaging modality that detects the spatial distribution of magnetic tracers with high resolution and sensitivity [1–5]. It has the potential for real-time, *in vivo* imaging of humans and animals. MPI works on the principle that the magnetic nanoparticle (MNP) tracers are periodically magnetized by a sinusoidal excitation field of frequency f (typically several tens of kHz). A pair of receive coils designed as gradiometers record the dynamic magnetic responses of tracers and remove the feed-through signals in real time. Due to the nonlinear magnetic responses of MNPs, higher harmonics at 3f, 5f, 7f, etc, are uniquely produced by the MNP tracers for the frequency-space (f-space) [6, 7] MPI image reconstruction. Tomographic imaging is achieved using a selection field with a magnetic gradient of several T/m [8–10], which selectively activates MNP tracers within a field-free region (FFR) at specific locations at each instantaneous time. MNP

tracers outside this FFR are magnetically saturated by the gradient field, resulting in negligible harmonics from these regions. By rastering the FFR through the field of view (FOV) along a pre-programmed trajectory, MNP tracers at different locations are sequentially activated. This allows for the reconstruction of a tracer-based MPI image [7, 11–13].

Based on the theory of MPI, the magnetic properties of MNP tracers and their relaxation times set the limit of imaging spatial resolution (i.e., intrinsic spatial resolution) [5, 14–16]. Researchers are actively applying different mathematical models to calculate the dynamic magnetizations of MNPs under fast-changing magnetic field(s) [17–19], i.e., the excitation field(s). Research has evolved from the traditional Langevin function that ignores the relaxation times of MNPs, to the more advanced stochastic Langevin function [20–23] and Fokker–Planck equation [24] that consider the coupled Brownian and Néel relaxations of MNPs. The newer, more advanced models have been cross-validated with experimental data with great accuracy [20, 22]. Nevertheless, most reported modeling works assume an ensemble of MNPs with identical magnetic core sizes and often ignore the surface non-magnetic coating layers. However, artificially synthesized MNPs exhibit a log-normal size distribution and, for the majority of applications, MNPs are surface-functionalized with non-magnetic coating layers (such as polymers or proteins) to enhance their colloidal stability [25]. It should be noted that the dynamic magnetizations of MNPs are largely affected by their magnetic core and hydrodynamic sizes [26, 27]. A uniformly sized ensemble and a non-uniformly sized ensemble of MNPs can exhibit very different collective magnetic responses under the same excitation field(s), even if these two ensembles of MNPs share identical average magnetic core sizes. Thus, a correct description of the magnetic responses of MNPs with various size distributions and non-magnetic shell layers is of paramount importance for moving this technology a step forward.

In this work, we systematically investigate the effect of MNP tracers' size distribution on their collective dynamic magnetizations and the point-spread functions (PSF) in MPI. Initially, we characterize the log-normal size distributions of four commercial MNP products, SHP15, SHP25, IPG30, and SHS30, using transmission electron microscopy (TEM) and determine their averaged magnetic core sizes (D_c) and intrinsic standard deviations (σ_0). To collect information on the surface non-magnetic coating layer thickness for these MNP products, their hydrodynamic sizes (area-based statistics method) are measured using dynamic light scattering (DLS). Subsequently, we model an ensemble of 10,000 non-interacting MNPs in an FFR, varying their size distribution (σ). We study the effect of size distribution by deteriorating ($\sigma = 3\sigma_0, 5\sigma_0, 7\sigma_0$, where σ_0 is the intrinsic standard deviation observed from TEM results) and improving ($\sigma = 0.5\sigma_0$) the size uniformity of these 10,000 MNP tracers, and we record their time-domain dynamic magnetizations (M-t curves), magnetization-field hysteresis loops (M-H curves), PSF, and higher harmonics. This study provides valuable insights into how the size distribution of MNP tracers can enhance or degrade the imaging performance of MPI.

2. Mathematical models, materials, and methods

2.1. Stochastic langevin model with coupled néel and brownian relaxations

Langevin function is the most widely recognized, classical approach for describing the magnetization of a non-interacting, isotropic, and identical ensemble of MNPs. It is only applicable under equilibrium approximation and does not account for noise in nanoparticle dynamics. In a more realistic scenario, where noise is considered, the stochastic Langevin model provides a better description of MNPs' magnetization dynamics [22, 23, 28]. It effectively captures the effects of Néel and Brownian relaxation times on magnetization dynamics by considering the combined rotational dynamics of both the nanoparticle's magnetic cores and surface coatings. In this context, the dynamic of an MNP with a hydrodynamic volume V_h ($=\frac{\pi}{6}D_h{}^3$, where D_h is hydrodynamic diameter) is described by the overall torque applied to its easy axis $\boldsymbol{n}$, and the evolution of internal magnetization $\mathbf{M}$ ($=M\boldsymbol{m}$, where $\boldsymbol{m}$ is the dimensionless unit magnetization vector) is governed by the Landau–Lifshitz-Gilbert (LLG) equation. A generalized torque and field are derived from the Helmholtz free energy equation, leading to a generalized form of the torque and field [22]. By incorporating thermal fluctuations into these torques and fields within the overall torque and LLG equations, the model results in coupled differential equations that account for Néel and Brownian relaxations. Moreover, the nanoparticle acceleration is neglected in this model due to the dominance of viscous forces [22]. Reforming the coupled differential equations, incorporating physical quantities such as Néel and Brownian relaxation times, the system can be described as follows:

$$\frac{d\boldsymbol{n}}{dt} = \frac{-1}{\tau_B}(\sigma_k(\boldsymbol{m} \cdot \boldsymbol{n})(\boldsymbol{m} \times \boldsymbol{n}) + \boldsymbol{\theta_{th}}) \times \boldsymbol{n} \tag{1}$$

$$\frac{d\boldsymbol{m}}{dt} = \frac{1}{\tau_0}\left(\frac{1}{\alpha}\boldsymbol{\xi} + \boldsymbol{m} \times \boldsymbol{\xi} + \frac{1}{\alpha}\boldsymbol{H_{th}} + \boldsymbol{m} \times \boldsymbol{H_{th}}\right) \times \boldsymbol{m} \tag{2}$$

Table 1. Variables and values that are used in this work.

Variable	Value	References
Viscosity (Pa·s)	0.001	—
Temperature (K)	300	—
Damping parameter α	1	[22]
Gyromagnetic Ratio γ (GHz/T)	176	[30]
Magnetic Anisotropy K_a (kJ/m^3)	3	[31, 32]
Saturation Magnetization M_S (kA/m)	480	[26]
Excitation Field Amplitude (mT/μ_0)	20	[5, 8, 19]
Excitation Field Frequency (kHz)	25	
Receive Coil Sensitivity (μT/A)	100	[33]
Gradient Field Magnitude (T/m)	3	[8–10]

where $\tau_B = \dfrac{3V_h\eta}{k_B T}$ is the Brownian relaxation time, $\tau_0 = \dfrac{\mu(1+\alpha^2)}{2k_B T\alpha\gamma}$ is the Néel attempting time which relates to the commonly known Néel relaxation time, $\sigma_k = \dfrac{K_a V_c}{k_B T}$ is the dimensionless anisotropy energy, $\boldsymbol{H_{th}}$ is the thermal noise equivalent field, $\boldsymbol{\theta_{th}}$ is the torque noise, and $\boldsymbol{\xi} = \dfrac{\mu_0\mu\boldsymbol{H}}{2} + \sigma_k(\boldsymbol{m}\cdot\boldsymbol{n})\boldsymbol{n}$ is the total field including $\boldsymbol{\xi'} = \dfrac{\mu_0\mu\boldsymbol{H}}{2}$ (the dimensionless excitation field that serves as the classical Langevin model argument) and $\sigma_k(\boldsymbol{m}\cdot\boldsymbol{n})\boldsymbol{n}$ (the dimensionless anisotropy field coupled with the magnetization). η and T are the viscosity and temperature of the solution, respectively, $\boldsymbol{H}$ is the excitation field, k_B is the Boltzmann constant, α is the damping parameter, γ is the gyromagnetic ratio, K_a is magnetic anisotropy constant, $V_c\left(=\dfrac{\pi}{6}D_c{}^3\right)$ is magnetic core volume, μ is the value of magnetic moment expressed as $\mu = M_s V_c$, and μ_0 is the vacuum permeability.

In the reported literature [18, 29], where the Langevin model $M = M_s L(\xi')$ was employed. The PSF was defined as the derivative of the magnetization model (i.e., Langevin function). Building on this approach, in this paper, we express the vector form of magnetization as $\boldsymbol{M} = M_s\boldsymbol{m}(\boldsymbol{\xi'}, \tau_0, \tau_B)$ and define the PSF as the derivative of the magnetization model **m** with respect to the dimensionless total field, $d\boldsymbol{m}/d\boldsymbol{\xi}$. This derivative accounts for the influence of anisotropy energy in the dynamic modeling of MNP magnetization. The anisotropy energy, impacted by MNP size, plays a critical role in determining the magnetization dynamics of MNPs.

The reduced form of correlation becomes equal to the Néel attempting time and Brownian relaxation time by:

$$\langle\boldsymbol{\theta_{th}^i}(t)\boldsymbol{\theta_{th}^j}(t')\rangle = \tau_B\delta_{ij}\delta(t-t') \tag{3}$$

$$\langle\boldsymbol{H_{th}^i}(t)\boldsymbol{H_{th}^j}(t')\rangle = \tau_0\delta_{ij}\delta(t-t') \tag{4}$$

In this study, we examine the dynamic magnetizations of four commercial iron oxide MNP products with varying size distributions, where the externally applied magnetic field $\boldsymbol{H}$ serves as the sole excitation field. We focus on the excitation field applied along the Z-axis and simulate the magnetic dynamics of 10,000 MNPs using standard numerical methods for the stochastic Langevin equation with the Stratonovich interpretation. The tracer core volume-weighted average dynamic magnetizations of MNPs along the excitation field direction, M_z, are recorded. The recording is done with a sampling frequency of 5 MHz, and the results are plotted as M-t curves. The real-time voltage signal is obtained from a receiver coil, based on Faraday's law of induction in a space that has been discretized into 3D voxels. The simplified equation for this voltage signal can be expressed as follows:

$$u(t) = -\mu_0 p_c \int_{-\infty}^{+\infty} p(r)\frac{\partial\bar{m}_z(r,t)}{\partial t}d^3r \tag{5}$$

where p_c represents the coil sensitivity, $p(r) = \sum_i^{10^4} V_i\delta(r-r_i)$ is the particle concentration, and $\bar{m}_z$ is the average weighted magnetization (average weighted with 10,000 different core sizes extracted from size distribution) in the Z-axis. Additionally, we assume that the MNPs concentration at the voxel's center and that the voxel is entirely within the FFR. Fast Fourier Transform (FFT) is applied and the signal, $u(t)$, and harmonics are obtained after removing the fundamental frequency component.

The dynamic magnetization versus the excitation field along the Z-axis during a few periods of the excitation field and after stabilization is plotted as M-H curves. From the M-H curves, we derive the PSF ($d\boldsymbol{m}/d\xi - \xi'$ curves). The full width at half maximum (FWHM) of the PSF is used as a parameter to evaluate the intrinsic spatial resolution in MPI systems, Δx, which can be determined by:
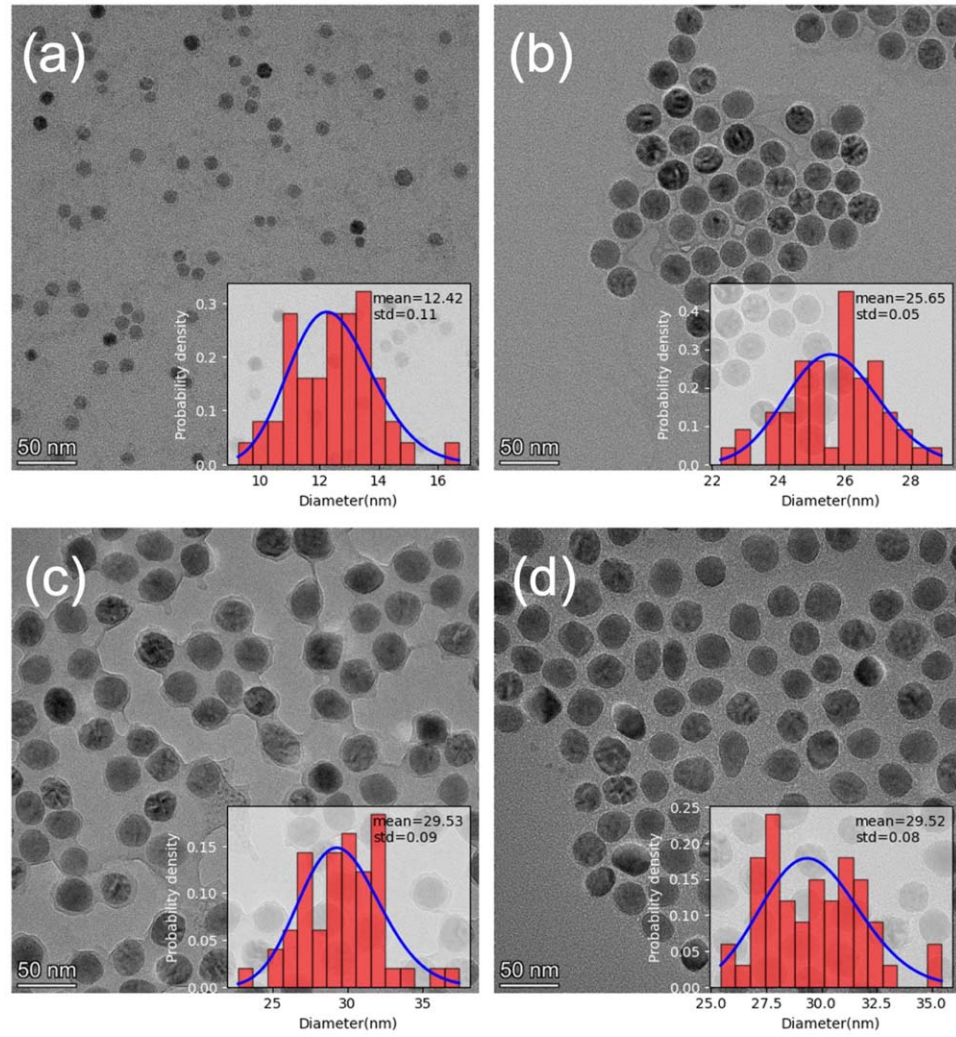
Figure 1. TEM images and histograms of magnetic core size distributions of (a) SHP15, (b) SHP25, (c) IPG30, and (d) SHS30 MNPs.

$$\Delta x = \frac{k_B T}{\mu_0 \mu G} \xi_{FWHM} \tag{6}$$

where G is the strength of the gradient field and ξ_{FWHM} is the FWHM that can be measured from the PSF curve. The magnetization evaluation over time is affected by the side lobes in the frequency domain, while the evaluation over the field is affected by a high magnetization ratio at saturation points. To mitigate these challenges, a Kaiser windowing technique followed by a Savitzky–Golay filter is further applied to $d\boldsymbol{m}/d\xi$ and $\frac{\partial \bar{m}_z(t)}{\partial t}$.

The parameters and values used in this work are summarized in table 1.

2.2. Iron oxide MNP products

The SHP15, SHP25, IPG30, and SHS30 MNPs (Ocean NanoTech, LLC) are single-core iron oxides with various core sizes and surface coatings [34]. SHP15 and SHP25 MNPs are coated with carboxylic acid groups and report average magnetic core sizes of 15 and 25 nm, respectively. Both SHP15 and SHP25 MNPs are suspended in DI water. IPG30 and SHS30 MNPs are iron oxides coated with protein G and streptavidin, respectively. Both have an average magnetic core size of 30 nm and are suspended in a 10 nM phosphate-buffered saline (PBS) solution with 0.01% BSA and 0.02% NaN_3. In our models, we assumed a viscosity of 1 cp (=0.001 Pa·s) for the solution.

2.3. Hydrodynamic size and morphological characterizations of MNPs

The hydrodynamic sizes of the MNPs were characterized by using a DLS particle size analyzer (Microtrac NANO-flex) at room temperature. Each MNP sample was 1 ml in volume and varying MNP concentrations from 0.25 to 0.5 mg ml^{-1}. TEM images, depicting the sizes and shapes of the MNPs, were obtained using the Thermo Fisher Talos F220X microscope operating at an accelerating voltage of 200 keV. TEM samples were
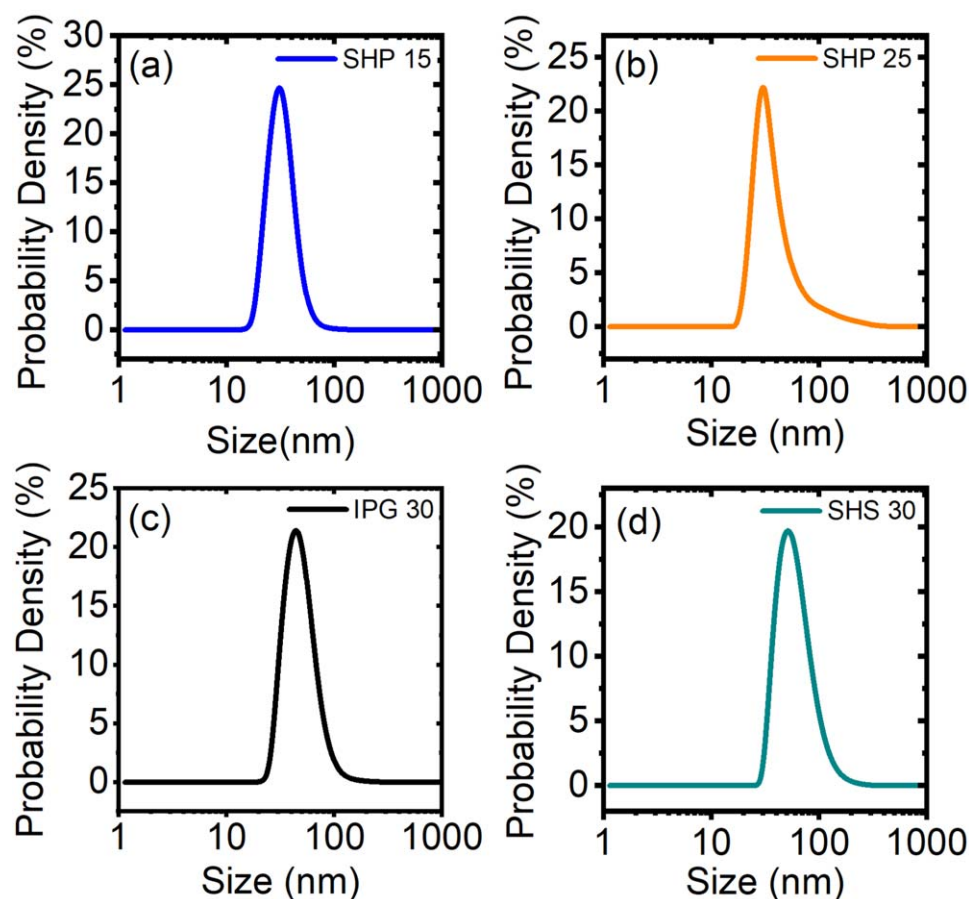
Figure 2. Probability density of hydrodynamic size distributions of (a) SHP15, (b) SHP25, (c) IPG30, and (d) SHS30 MNPs. Data is plotted based on area-weighted DLS distribution.

Table 2. Summary of the magnetic core sizes and non-magnetic coating layer thicknesses of SHP15, SHP25, IPG30, and SHS30 MNPs.

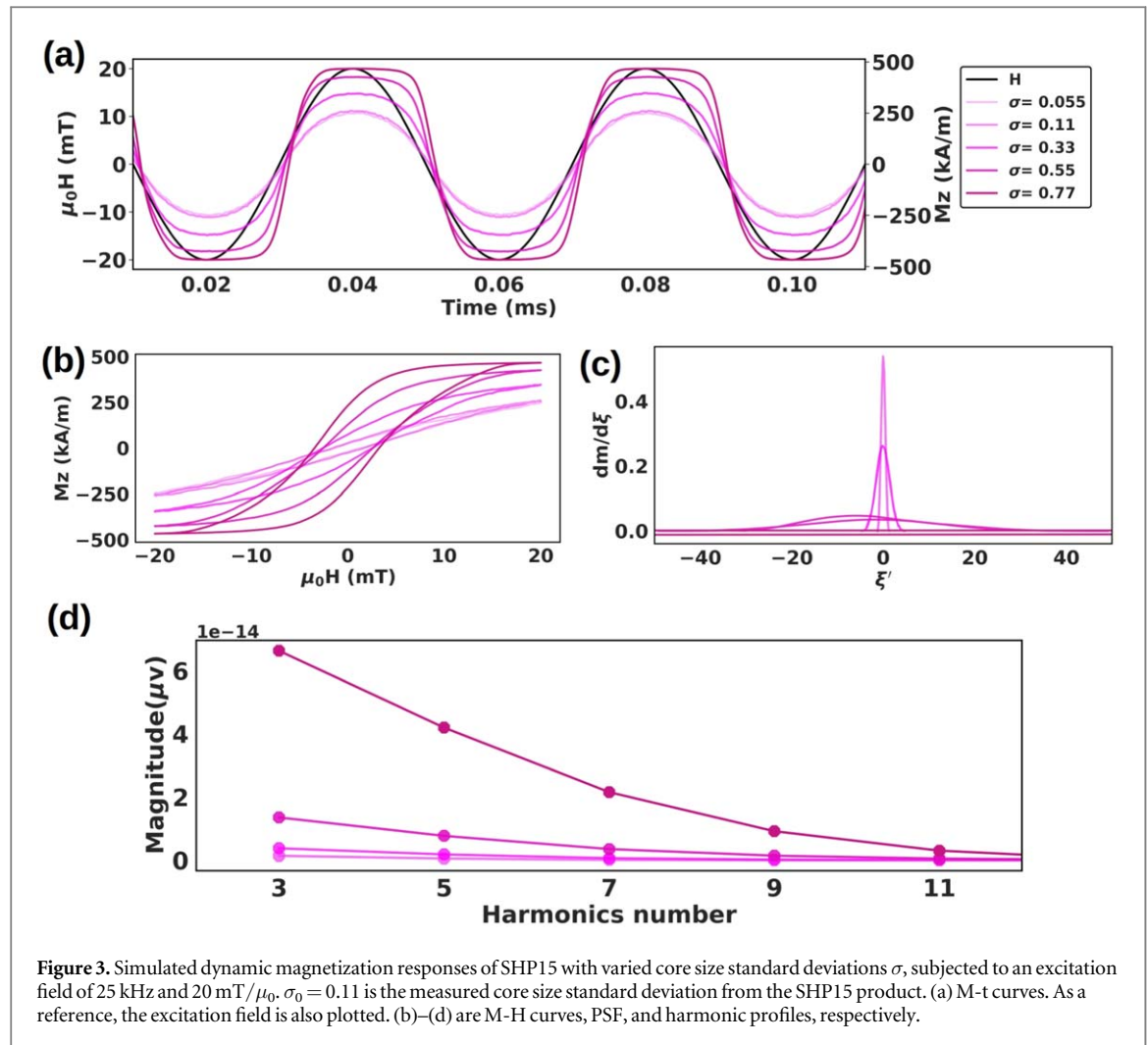| MNP	Magnetic core size		Hydrodynamic size	
	Average (D_c)	Standard deviation (σ_0)	Average (D_h)	Coating thickness (d)
SHP15	12.42 nm	0.11	30.40 nm	9.0 nm
SHP25	25.65 nm	0.05	41.10 nm	7.7 nm
IPG30	29.53 nm	0.09	45.90 nm	8.2 nm
SHS30	29.52 nm	0.08	57.70 nm	14.1 nm

prepared by drop-casting 10 μl of MNP suspensions onto carbon-coated Cu TEM grids (Ted Pella, Inc.) and allowing them to air-dry at room temperature before characterization.

3. Results and discussion

3.1. Experimentally observed size distribution of MNP products

Figures 1(a)–(d) shows the TEM images of SHP15, SHP25, IPG30, and SHS30 MNPs, respectively. The magnetic core sizes of the MNPs were calculated under the assumption that all MNPs were perfectly spherical. The bar chart illustrates the core size distribution (diameter) of 50 MNPs randomly selected from the TEM images for each MNP product. The size distribution curves were fitted using a log-normal function. The average magnetic core size (D_c) and intrinsic standard deviation (σ_0) for each MNP product are summarized in table 2.

The area-based hydrodynamic size distributions of the MNPs were obtained via DLS, fitted using a log-normal function, and presented in figures 2(a)–(d). The average hydrodynamic sizes of the four MNP products are calculated and summarized in table 2. In this work, we calculated the non-magnetic coating layer thickness (d) for each MNP product by using the differences in average hydrodynamic size (D_h) and average magnetic core

Figure 3. Simulated dynamic magnetization responses of SHP15 with varied core size standard deviations σ, subjected to an excitation field of 25 kHz and 20 mT/μ_0. $\sigma_0 = 0.11$ is the measured core size standard deviation from the SHP15 product. (a) M-t curves. As a reference, the excitation field is also plotted. (b)–(d) are M-H curves, PSF, and harmonic profiles, respectively.

size (D_c). As shown in the last column of table 2, SHP15, SHP25, and IPG30 have similar coating layer thicknesses ranging from 7.7 to 9 nm, while SHS30 has a thicker coating layer of 14.1 nm.

To study the effect of the non-magnetic coating layer on the MPI performance for MNP tracers with varying core size distributions, we collectively assumed an 8 nm thick coating layer for SHP15, SHP25, and IPG30 in our models. For SHS30, we assumed a 14 nm thick coating layer.

3.2. Mathematical modeling: the effect of tracer size distribution on MPI performance

In this work, we are only interested in studying the effect of MNP tracer size distribution on the MPI performance. When modeling the dynamic magnetizations of an ensemble of 10,000 MNPs subjected to an excitation field, the standard deviation of tracers' core sizes is varied while the average core size is fixed. This step will introduce MNP tracers with different core sizes (deviations from the average core size). We are aware that the intrinsic magnetic properties of MNPs, such as saturation magnetizations, magnetic anisotropy, blocking temperature, superparamagnetism, etc, are affected by the magnetic core sizes [26]. However, this will inevitably make the system complicated and diminish the direct effect of tracer size distribution, i.e., the standard deviation of core size σ. Since the intrinsic magnetic properties of MNPs can vary widely due to different synthesis methods, degrees of oxidation, uncontrollable crystalline defects, and shapes of nanoparticles [26]. Even MNPs with the same magnetic core materials, same core sizes, and same synthesis method can show very different magnetic properties. For instance, the reported effective magnetic anisotropy values for iron oxide MNPs with core sizes less than 100 nm range from 1 to 10 kJ m^{-3} [31, 32]. The reported saturation magnetization values can range from near zero up to the bulk iron oxide's M_S values of 400–525 kA m^{-1} [26]. Even for the same batch of MNPs, different storage environments can cause oxidation, altering their magnetic properties over time. Considering this variability and the storage history of MNPs, our models collectively assume a saturation magnetization M_S of 480 kA m^{-1} and an effective anisotropy K_a of 3 kJ m^{-3} for all MNP tracers. Adopting fixed saturation magnetization and anisotropy values in our model ensures that tracer core size distribution (varying standard deviations) is the only contributor to the varying results we collected.

Table 3. Summary of the relaxation times and FWHM obtained from the PSFs of SHP15, SHP25, IPG30, and SHS30 MNPs with varying core size standard deviation (σ). A log-normal core size distribution was assumed for an ensemble of 10,000 MNPs in FFR.

MNP	σ	τ_B (mean value in s)	τ_0 (mean value in s)	FWHM[a]
SHP15	0.055	8.76e-6	4.23e-10	1.03
	0.11 (σ_0)	8.86e-6	4.38e-10	1.16
	0.33	1.02e-5	7.04e-10	3.86
	0.55	1.50e-5	1.92e-9	46.23
	0.77	1.4e-4	5.94e-8	1319.39
SHP25	0.025	2.74e-5	3.64e-9	6.99
	0.05 (σ_0)	2.77e-5	3.70e-9	7.19
	0.15	2.91e-5	4.10e-9	9.38
	0.25	3.14e-5	4.87e-9	15.41
	0.35	4.72e-4	1.02e-8	32.88
IPG30	0.045	3.60e-5	5.61e-9	10.41
	0.09 (σ_0)	3.64e-5	5.73e-9	11.86
	0.27	4.20e-5	7.58e-9	30.26
	0.45	5.88e-5	1.35e-8	121.29
	0.63	5.06e-4	2.31e-7	1209.26
SHS30	0.04	7.25e-5	5.60e-9	10.34
	0.08 (σ_0)	7.29e-5	5.71e-9	11.51
	0.24	7.84e-5	7.03e-9	20.93
	0.4	9.60e-5	1.15e-8	100.21
	0.56	2.54e-4	7.00e-8	378.82

[a] The FWHM is dimensionless because ξ' is dimensionless. Scaling to Tesla can be achieved by adjusting ξ'.

3.2.1. SHP15 MNPs with varying size distributions

Based on the TEM and DLS results, the SHP15 MNP product shows an average magnetic core size of $D_c = 12.42$ nm with an intrinsic standard deviation of $\sigma_0 = 0.11$ and an average hydrodynamic size of $D_h = 30.40$ nm. Herein, in our mathematical model, we assumed 10,000 non-interacting SHP15 MNPs with an average magnetic core size of $D_c = 12.42$ nm, a non-magnetic coating layer thickness d = 8 nm, with varying degrees of core size uniformity where the standard deviations of core size studied were $\sigma = 0.055$ ($0.5\sigma_0$), 0.11 (intrinsic σ_0), 0.33 ($3\sigma_0$), 0.55 ($5\sigma_0$), and 0.77 ($7\sigma_0$).

The small magnetic core size of SHP15 MNPs limits their response to the excitation field, resulting in a sinusoidal shape M-t curve and linear magnetization hysteresis, as shown in figures 3(a) and (b). A larger standard deviation (σ) from the mean core size of 12.42 nm increases the overall effective core size of the MNP ensemble, enhancing the net magnetic moment. This enhancement transforms the sinusoidal M-t curve into a square-shaped curve and the linear hysteresis into a more non-linear hysteresis, as observed in figures 3(a) & (b). The increased net size of the MNPs increases the Néel attempting time, introducing a phase delay in response to the excitation field (figure 3(a)) and widening the hysteresis loop (figure 3(b)). Additionally, larger size deviations increase the anisotropy energy along the easy axis (ξ), disrupting the MNPs' response to the excitation field and reducing the PSF peaks, as illustrated in figure 3(c). Furthermore, the increased nonlinearity in the MNPs' magnetization response strengthens harmonic signals. Although these harmonics are partially diminished by dominant relaxation effects, they are amplified with higher particle concentrations and greater size deviations. Consequently, larger size deviations result in stronger harmonic signals, as depicted in figure 3(d). Data on Brownian relaxation time, Néel attempting time, and FWHM are summarized in table 3.

3.2.2. SHP25 MNPs with varying size distributions

The TEM and DLS results show that SHP25 MNPs have an average core size of $D_c = 25.65$ nm with an intrinsic standard deviation of $\sigma_0 = 0.05$, coated by a 7.7 nm thick carboxylic acid layer. For a side-by-side comparison between SHP15 and SHP25 MNPs, in our models, we assumed a coating layer thickness of 8 nm for both SHP15 and SHP25 MNP tracers.

SHP25, with a larger average core size compared to SHP15, exhibits square-shaped monetization signal and nonlinear hysteresis and reaches saturation at a field of 20 mT/μ_0, as shown in figures 4(a) and (b). The larger average core size also leads to lower PSF peaks, even with smaller standard deviations, as illustrated in figure 4(c). Additionally, the increased average core size enhances the nonlinearity of the MNPs' response to the excitation field, resulting in stronger harmonic signals, as depicted in figure 4(d). For SHP25, variations in standard
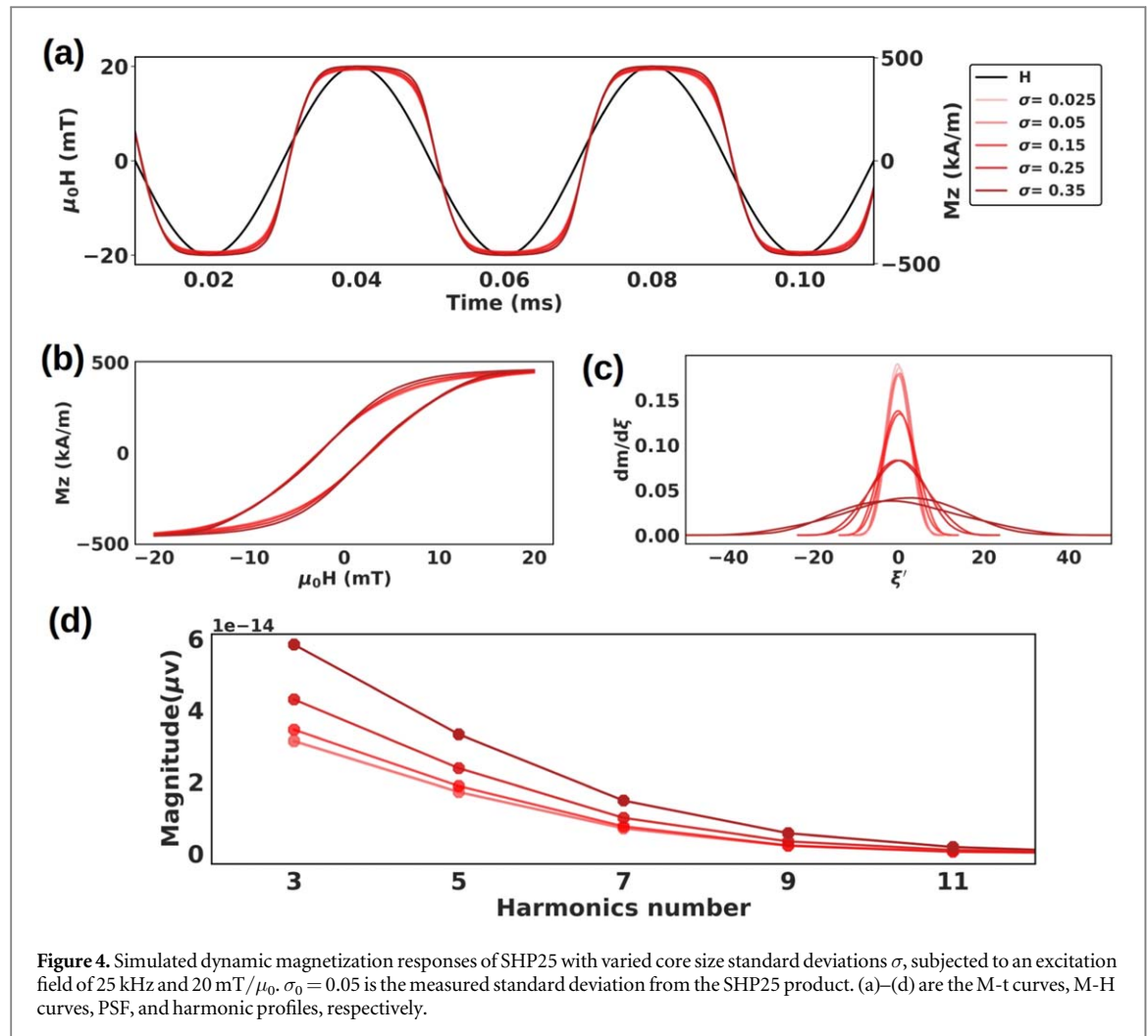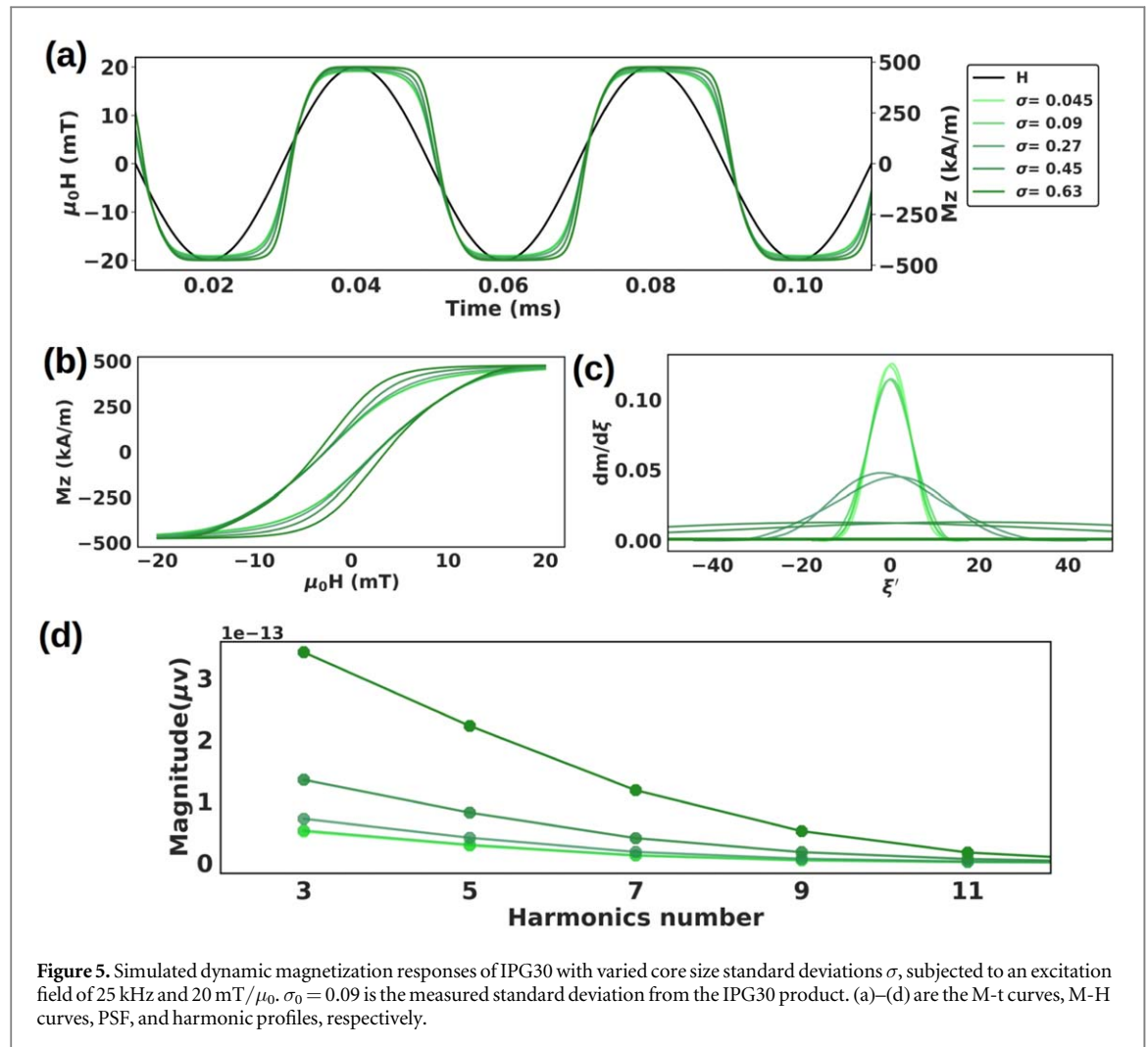
Figure 4. Simulated dynamic magnetization responses of SHP25 with varied core size standard deviations σ, subjected to an excitation field of 25 kHz and 20 mT/μ_0. $\sigma_0 = 0.05$ is the measured standard deviation from the SHP25 product. (a)–(d) are the M-t curves, M-H curves, PSF, and harmonic profiles, respectively.

deviation (σ), ranging from 0.025 to 0.35, produce only subtle changes in the M-t and M-H curves (figures 4(a) and (b)) compared to SHP15. Similar to SHP15, larger size deviations in SHP25 increase anisotropy energy along the easy axis, disrupting the response to the excitation field and reducing PSF peaks (figure 4(c)). However, this reduction is smaller in SHP25 due to smaller variations in size deviations. Furthermore, as with SHP15, larger size deviations in SHP25 increase the net ensemble size and magnetic moment, leading to an enhancement in harmonic signals (figure 4(d)). For the largest standard deviations in both SHP15 and SHP25, the net ensemble size and magnetic moment become comparable, resulting in similar harmonic strengths (figures 3(d) and 4(d)). In summary, a larger average core size reduces PSF peaks and enhances harmonics, while greater size deviations further amplify harmonics and dramatically reduce PSF peaks.

3.2.3. IPG30 MNPs with varying size distributions

The TEM and DLS results show that the average magnetic core size, core size standard deviation, and average coating layer thickness for IPG30 are $D_c = 29.53$ nm, $\sigma_0 = 0.09$, and $d = 8.2$ nm, respectively. In our model, we assumed a coating thickness of $d = 8$ nm for IPG30 MNPs.

The IGP30, with a larger core size than SHP25 but the same coating thickness, exhibits an enhanced response to the applied field, like SHP25. The increased core size extends the MNP response to the excitation field, resulting in a square-shaped M-t curve and a nonlinear M-H curve that saturates at 20 mT/μ_0 (figures 5(a) and (b)). Furthermore, the increase in average core size extends the Néel relaxation time, leading to a greater phase delay in the M-t curve and wider hysteresis loops (figures 5(a) and (b)). Additionally, the larger core size reduces PSF peaks and strengthens harmonic signals compared to SHP25, as shown in figures 5(c) and (d). Like SHP15 and SHP25, a larger standard deviation in IGP30 reduces PSF peaks due to increased anisotropy energy and enhances harmonic strength due to the larger net ensemble core size and magnetic moment. However, the greater variability in size deviations in IGP30, compared to SHP25, results in a more significant reduction in PSF peaks.
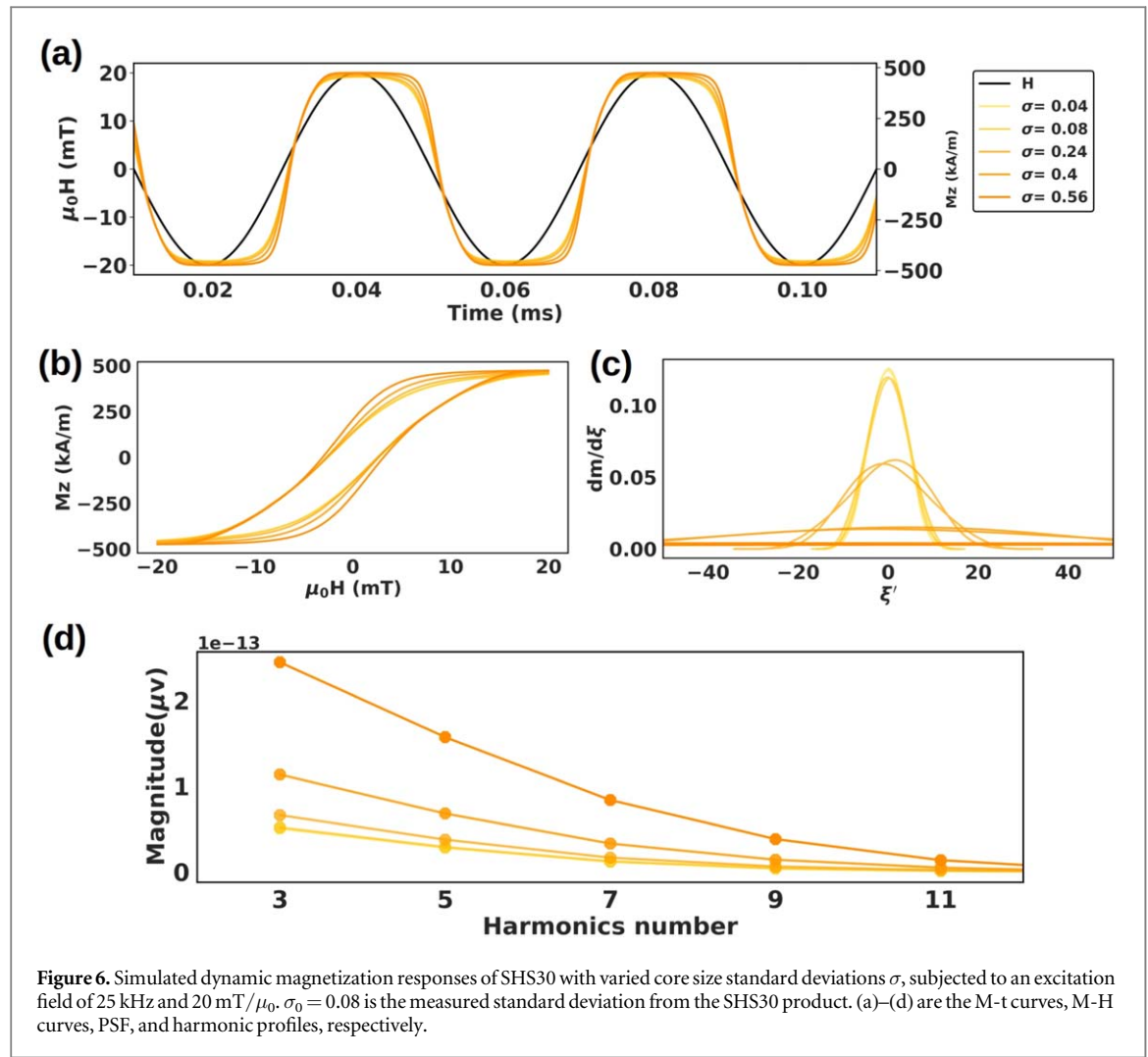
Figure 5. Simulated dynamic magnetization responses of IPG30 with varied core size standard deviations σ, subjected to an excitation field of 25 kHz and 20 mT/μ_0. $\sigma_0 = 0.09$ is the measured standard deviation from the IPG30 product. (a)–(d) are the M-t curves, M-H curves, PSF, and harmonic profiles, respectively.

3.2.4. SHS30 MNPs with varying size distributions

The TEM and DLS results show that the average magnetic core size, core size standard deviation, and average coating layer thickness for SHS30 MNPs are $D_c = 29.52$ nm, $\sigma_0 = 0.08$, and d = 14.1 nm, respectively. In our model, we assumed a coating thickness of 14 nm for SHS30 MNPs.

SHS30 exhibits a thicker coating layer while maintaining the same core size as IGP30. The effects of core size and its deviations, when compared to SHP25, mirror those observed in IGP30. Compared to SHP25 and SHP15, a larger average core size improves the SHS30 MNPs' response to the field, resulting in a square-shaped M-t curve and nonlinear hysteresis (figures 5(a) and (b)). The extended Néel attempting time causes phase lag in the M-t curve and wider hysteresis loops. Additionally, the larger average core size reduces PSF peaks, increases the net ensemble size and magnetic moment, and enhances harmonics. Greater size deviation further reduces PSF peaks and amplifies harmonics. A larger coating size has a minimal impact on PSF peaks and results in a subtle reduction in harmonics compared to IGP30 (figures 5(d) and 6(d)).

4. Conclusions

The size of the MNP tracer, including the core and the coating, is one of the most important properties in MPI imaging systems. In most models and experiments, it is assumed that all tracers are the same size. However, this assumption is not correct because the size of the particles is lognormally distributed. In this respect, the effect of size distribution is completely ignored in both experimental and modeling works. To evaluate the effect of the MNP tracer size distribution on the MPI application, we used a stochastic Langevin function with coupled Brownian-Néel relaxation models to simulate the dynamic magnetization responses of MNP tracers. In the FFR, an ensemble of 10,000 non-interacting MNP tracers exposed to an excitation field of 25 kHz and 20 mT/μ_0 was assumed. The mean and standard deviation of the core size, as well as the mean hydrodynamic size, for the four commercial iron oxide MNP products - SHP15, SHP30, IGP30, and SHS30 - were obtained from the TEM and

Figure 6. Simulated dynamic magnetization responses of SHS30 with varied core size standard deviations σ, subjected to an excitation field of 25 kHz and 20 mT/μ_0. $\sigma_0 = 0.08$ is the measured standard deviation from the SHS30 product. (a)–(d) are the M-t curves, M-H curves, PSF, and harmonic profiles, respectively.

DLS results. A few variations in the core size standard deviation, summarized in table 3, were considered for each sample to investigate the effect of tracer size distribution on MPI performance.

For smaller MNPs like SHP15, size deviation plays a crucial role in altering magnetization behavior. Larger size deviations increase the magnetic moments of the particles, which outweigh the effects of anisotropy energy (for small anisotropy constant) at the direction of the easy axis. This enhancement in collective magnetic moments strengthens the ensemble's response to the excitation field, transforming sinusoidal signals into square-like M-t curves and linear M-H curves into nonlinear. These changes improve SNR. However, the increased anisotropy energy disrupts the response to the excitation field, significantly reducing PSF peaks and degrading imaging resolution. In SHP25, a larger core size enhances the magnetization response, exhibiting greater nonlinearity compared to SHP15. It also increases the Néel relaxation time, leading to wider hysteresis loops and stronger harmonic generation. Despite these benefits, larger average core size reduces PSF peaks. Like SHP15, a larger size deviation in SHP25 amplifies harmonics by boosting the collective magnetic moment while increasing anisotropy energy, further diminishing PSF peaks and degrading imaging resolution. IGP30 and SHS30 demonstrate similar trends. Larger core sizes improve SNR and reduce PSF peaks, while larger size deviations further enhance SNR and reduce imaging resolution. Notably, the impact of coating layer thickness, by comparing IPG30 and SHS30, is negligible. Overall, larger core sizes and size deviations enhance SNR and harmonic strength but come at the cost of reduced PSF peaks and imaging resolution.

The average M_z component for 10,000 MNPs is lower than the M_s value of 480 kA m^{-1} due to the coupling of the field and other components. In this study, a low anisotropy constant is used because, when multiplied with particle size and large size deviations, it could result in a high anisotropy energy that significantly disrupts the particle's response to the excitation field. If the model encounters high anisotropy energy, magnetization may collapse due to Brownian-dominated dynamics [35] or the anisotropy energy barrier. In such situations, increasing the excitation field and MNP concentration, or using materials with higher saturation magnetization can be effective. However, studying MNP size distribution becomes challenging, as the root cause of magnetization collapse may not be apparent. In this respect, to facilitate a more practical investigation of particle

size distribution, we utilized a low anisotropy constant, which allowed us to observe a significant magnetization response and effectively study the influence of particle size distribution in this context.

Our findings offer valuable guidance for researchers synthesizing MNP tracers for MPI applications, particularly regarding optimal size for clinical use. For longer blood circulation times, tracers between 10 and 100 nm are preferred, as this range avoids rapid kidney clearance of smaller particles (<10 nm) and reduces uptake by the liver and spleen, which often capture larger particles (>200 nm) through the reticuloendothelial system. Among the MNP tracers studied here (SHP15, SHP25, IPG30, and SHS30), The SHS15 tracers exhibited the smallest FWHM at narrower particle size deviations, offering the highest spatial resolution in imaging. However, achieving an adequate SNR requires using these small MNPs at a high concentration.

Acknowledgments

Data availability statement

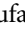All data that support the findings of this study are included within the article (and any supplementary files).
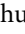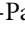
Author contributions

C L, J G-P, R H, and K W conceived the presented idea and designed the modeling. E A developed the theory, performed the computations, and plotted figures 3–6. B R, S M, and K W verified the models. S L and V K C carried out the TEM and DLS experiments and wrote sections 2.2, 2.3, and 3.1. B R and S M supported the writing of section 3.1 and prepared table 2, figures 1 and 2. Y A W prepared the MNPs and interpreted the results in section 3.1. E A and K W. co-led the writing of sections 1, 2.1, 3.2, and 4. J-P W, C L, J G-P, and R H interpreted the results in section 3.2 and proofread the paper. J-P W and K W secured the funding. All authors discussed the results and contributed to the final manuscript.

Notes

The author declares no conflict of interest.

ORCID iDs

Ebrahim Azizi ⬤ https://orcid.org/0000-0002-0230-2534
Bahareh Rezaei ⬤ https://orcid.org/0000-0003-3446-3559
Shahriar Mostufa ⬤ https://orcid.org/0000-0002-3326-4817
Shuang Liang ⬤ https://orcid.org/0000-0003-1491-2839
Vinit Kumar Chugh ⬤ https://orcid.org/0000-0001-7818-7811
Jian-Ping Wang ⬤ https://orcid.org/0000-0003-2815-6624
Changzhi Li ⬤ https://orcid.org/0000-0003-2188-4506
Jenifer Gómez-Pastora ⬤ https://orcid.org/0000-0002-5157-4130
Rui He ⬤ https://orcid.org/0000-0002-2368-7269
Kai Wu ⬤ https://orcid.org/0000-0002-9444-6112

References

[1] Bakenecker A C, Ahlborg M, Debbeler C, Kaethner C, Buzug T M and Lüdtke-Buzug K 2018 Magnetic particle imaging in vascular medicine *Innov. Surg. Sci.* **3** 179–92
[2] Bauer L M, Situ S F, Griswold M A and Samia A C S 2015 Magnetic particle imaging tracers: state-of-the-art and future directions *J. Phys. Chem. Lett.* **6** 2509–17
[3] Gleich B and Weizenecker J 2005 Tomographic imaging using the nonlinear response of magnetic particles *Nature* **435** 1214–7

[4] Rezaei B *et al* 2024 Magnetic nanoparticles for magnetic particle imaging (MPI): design and applications *Nanoscale* **16** 11802–24

[5] Knopp T and Buzug T M 2012 *Magnetic Particle Imaging: An Introduction to Imaging Principles and Scanner Instrumentation* (Springer Science & Business Media)

[6] Knopp T, Rahmer J, Sattel T F, Biederer S, Weizenecker J, Gleich B, Borgert J and Buzug T M 2010 Weighted iterative reconstruction for magnetic particle imaging *Phys. Med. Biol.* **55** 1577–89

[7] Knopp T, Sattel T F, Biederer S, Rahmer J, Weizenecker J, Gleich B, Borgert J and Buzug T M 2010 Model-based reconstruction for magnetic particle imaging *IEEE Trans. Med. Imaging* **29** 12–8

[8] Tay Z W, Hensley D W, Chandrasekharan P, Zheng B and Conolly S M 2020 Optimization of drive parameters for resolution, sensitivity and safety in magnetic particle imaging *IEEE Trans. Med. Imaging* **39** 1724–34

[9] Goodwill P W, Konkle J J, Zheng B, Saritas E U and Conolly S M 2012 Projection x-space magnetic particle imaging *IEEE Trans. Med. Imaging* **31** 1076–85

[10] Vogel P, Rückert M A, Klauer P, Kullmann W H, Jakob P M and Behr V C 2013 Traveling wave magnetic particle imaging *IEEE Trans. Med. Imaging* **33** 400–7

[11] Grüttner M, Knopp T, Franke J, Heidenreich M, Rahmer J, Halkola A, Kaethner C, Borgert J and Buzug T M 2013 On the formulation of the image reconstruction problem in magnetic particle imaging *Biomed. Tech. Eng.* **58** 583–91

[12] Szwargulski P, Moddel M, Gdaniec N and Knopp T 2019 Efficient joint image reconstruction of multi-patch data reusing a single system matrix in magnetic particle imaging *IEEE Trans. Med. Imaging* **38** 932–44

[13] Chen X, Jiang Z, Han X, Wang X and Tang X 2021 The reconstruction of magnetic particle imaging: current approaches based on the system matrix *Diagnostics* **11** 773

[14] Ferguson R M, Khandhar A P and Krishnan K M 2012 Tracer design for magnetic particle imaging *J. Appl. Phys.* **111** 07B318

[15] Goodwill P, Tamrazian A, Croft L, Lu C, Johnson E, Pidaparthi R, Ferguson R, Khandhar A, Krishnan K and Conolly S 2011 Ferrohydrodynamic relaxometry for magnetic particle imaging *Appl. Phys. Lett.* **98** 262502

[16] Rahmer J, Weizenecker J, Gleich B and Borgert J 2009 Signal encoding in magnetic particle imaging: properties of the system function *BMC Med. Imaging* **9** 4

[17] Yari P, Chugh V K, Saha R, Tonini D, Rezaei B, Mostufa S, Xu K, Wang J-P and Wu K 2023 Static and dynamic magnetization models of magnetic nanoparticles: an appraisal *Phys. Scr.* **98** 082002

[18] Shasha C and Krishnan K M 2021 Nonequilibrium dynamics of magnetic nanoparticles with applications in biomedicine *Adv. Mater.* **33** 1904131

[19] Wu K *et al* 2024 Roadmap on magnetic nanoparticles in nanomedicine *Nanotechnology* **36** 042003

[20] Shah S A, Reeves D B, Ferguson R M, Weaver J B and Krishnan K M 2015 Mixed Brownian alignment and néel rotations in superparamagnetic iron oxide nanoparticle suspensions driven by an ac field *Phys. Rev.* B **92** 094438

[21] Reeves D B and Weaver J B 2012 Simulations of magnetic nanoparticle Brownian motion *J. Appl. Phys.* **112** 124311

[22] Reeves D B and Weaver J B 2015 Combined Néel and Brown rotational langevin dynamics in magnetic particle imaging, sensing, and therapy *Appl. Phys. Lett.* **107** 223106

[23] Usov N and Liubimov B Y 2012 Dynamics of magnetic nanoparticle in a viscous liquid: application to magnetic nanoparticle hyperthermia *J. Appl. Phys.* **112** 023901

[24] Weizenecker J 2018 The fokker–planck equation for coupled brown–néel-rotation *Phys. Med. Biol.* **63** 035004

[25] Rezaei B *et al* 2024 Effect of polymer and cell membrane coatings on theranostic applications of nanoparticles: a review *Adv. Healthc. Mater.* **13** 2401213

[26] Wu K, Su D, Liu J, Saha R and Wang J-P 2019 Magnetic nanoparticles in nanomedicine: a review of recent advances *Nanotechnology* **30** 502003

[27] Liu J, Su D, Wu K and Wang J-P 2020 High-moment magnetic nanoparticles *J. Nanoparticle Res.* **22** 1–16

[28] Anon Shah S A, Reeves D B, Ferguson R M, Weaver J B and Krishnan K M 2015 Mixed Brownian alignment and Néel rotations in superparamagnetic iron oxide nanoparticle suspensions driven by an ac field *Phys. Rev.* B **92** 094438

[29] Goodwill P W and Conolly S M 2011 Multidimensional x-space magnetic particle imaging *IEEE Trans. Med. Imaging* **30** 1581–90

[30] Kluth T 2018 Mathematical models for magnetic particle imaging *Inverse Probl.* **34** 083001

[31] Ludwig F, Remmer H, Kuhlmann C, Wawrzik T, Arami H, Ferguson R M and Krishnan K M 2014 Self-consistent magnetic properties of magnetite tracers optimized for magnetic particle imaging measured by ac susceptometry, magnetorelaxometry and magnetic particle spectroscopy *J. Magn. Magn. Mater.* **360** 169–73

[32] Eberbeck D, Dennis C L, Huls N F, Krycka K L, Gruttner C and Westphal F 2012 Multicore magnetic nanoparticles for magnetic particle imaging *IEEE Trans. Magn.* **49** 269–74

[33] Weizenecker J, Gleich B, Rahmer J, Dahnke H and Borgert J 2009 Three-dimensional real-time *in vivo* magnetic particle imaging *Phys. Med. Biol.* **54** L1

[34] Wu K, Liu J, Saha R, Peng C, Su D, Wang Y A and Wang J-P 2021 Investigation of commercial iron oxide nanoparticles: structural and magnetic property characterization *ACS Omega* **6** 6274–83

[35] Yoshida T and Enpuku K 2024 Field-dependent Néel relaxation time of magnetic nanoparticles in AC excitation fields: boundary field between Néel- and Brownian-dominant regions *J. Appl. Phys.* **135** 093901